Contents lists available at ScienceDirect

Materials Today Energy

Sustainable repurpose of waste melamine foam into bifunctional catalysts for efficient CO_2 capture and conversion

Fei-Feng Mao [a], Yu-Hua Dong [b], Yan Zhou [a, ***], Ming-Shuai Sun [a], Wei Hui [a, b, **], Duan-jian Tao [a, *]

[a] National Engineering Research Center for Carbohydrate Synthesis, Key Laboratory of Fluorine and Silicon for Energy Materials and Chemistry of Ministry of Education, School of Chemical Engineering, Jiangxi Normal University, Nanchang 330022, China
[b] School of Life Science, Jinggangshan University, Ji'an 343009, China

ARTICLE INFO

ABSTRACT

Global climate change has driven the scientific community to improve the utilization of a critical C1 resource carbon dioxide (CO_2) through carbon capture utilization (CCU) technology. The cycloaddition of CO_2 with epoxides provides perfect atom economy and economic feasibility to produce versatile cyclic carbonates used in various industries. However, the stable nature of CO_2 and epoxides requires highly active catalysts. In this work, the repurpose of nitrogenous waste melamine foams (MFs) as high-performance catalysts for the cycloaddition of CO_2 was explored. The pyrolyzed MF was modified with Cu to prepare a series of acid-base bifunctional porous catalysts (MFC-X-Cu). The results demonstrate that the acid-base synergy of the MFC-X-Cu catalysts increases the efficiency of the cycloaddition of various epoxides, yielding target products at 96—99% under mild conditions. Moreover, the characterization results revealed that the superior performance of MFC-X-Cu stems from its hollow structure and acid-base synergy, which are derived from nitrogen species in the repurposed MF and the post-modified copper component. The catalyst maintained consistent catalytic efficiency over five cycles, highlighting its strong recyclability. This work presents an eco-friendly and sustainable approach towards carbon neutrality by utilizing modified waste materials for CO_2 conversion into high-value chemicals.

1. Introduction

The greenhouse effect caused by carbon dioxide (CO_2) is recognized as a significant threat to global climate stability, prompting nations to adopt carbon-neutral policies to achieve long-term climate stabilization and sustainable development goals [1,2]. In response, the scientific community is devoting efforts to the implementation of carbon capture utilization (CCU) to enhance and optimize the efficiency of CO_2 utilization, thereby fostering global climate stability [3—6]. Notably, the cycloaddition of CO_2 with epoxides has emerged as a key process [7—9], distinguished by its 100% atom economy and economic sustainability. Furthermore, the resultant cyclic carbonate products are highly versatile, with applications spanning electric vehicle batteries, pharmaceuticals, and specialty chemicals [10,11]. However, the inherent thermodynamic stability of both CO_2 and epoxides poses significant challenges for their activation and conversion. Therefore, the development of highly active catalysts aligned with the carbon-neutral strategy is an up-and-coming for application of C1 resource in the present world.

In pursuit of enhanced economic returns and sustainable progress, the repurposing of nitrogen-containing waste from natural ecosystems and human activities has emerged as an intriguing and vital field of study for researchers. For example, biochar derived from N-rich biomass and proteins from animals and plants is converted through simple pyrolysis, gasification, and liquefaction processes, and serves as catalysts or catalyst supports [12—14]. Likewise, the residual coffee grounds and tea leaves from human consumption are repurposed into porous carbon materials through the above process, opening up diverse applications in gas absorption, catalysis, and electrochemical energy storage [15—17].

Meanwhile, melamine foam (MF) is recognized for its exceptional acoustic performance, thermal insulation, and lightweight properties, making it widely employed across various industries such as construction, transportation, electronics, and household appliances [18,19]. However, the disposal of resulting waste materials creates a huge environmental challenge. Notably, MF is naturally rich in nitrogen (N) and carbon (C), offering new opportunities for the innovative repurposing of this material. The N-doped strategy is a prominent approach to introducing basic sites for the modification of carbon materials [20–22]. For example, Sun et al. have demonstrated the effectiveness of N-doped carbon catalysts with different groups on their surface in catalyzing the cycloaddition reaction between CO_2 and various epoxides [23]. In addition, Zhang and co-workers synthesized N-doped carbon materials with different N species and doping amounts and studied the electrocatalytic reduction of CO_2 in different types of N-modified carbon materials [24]. However, the practical application of similar N-doped carbon materials is somewhat limited by the necessity of incorporating an additional nitrogen source. Hence, the natural advantage of MF pyrolysis lies in its ability to produce N-rich functional carbon materials without the need for additional N sources.

Our previous research has shown that pyrolyzed MF materials contain multiple basic sites of weak, medium, and strong basicity, which provide great modification environments for anchoring metals [25]. Thus, we envision grafting Lewis acidic sites onto the MF materials using a post-modified method to enhance their activation ability toward the reactant substrates of epoxides and CO_2. In the realm of heterogeneous catalysis, copper-based catalyst surfaces are frequently endowed with Lewis acidic sites, which facilitate the catalysis of reactions with high efficiency [26–28]. Herein, the waste MF was used as catalyst support and then post-modified with copper component to prepare a series of acid-base porous catalysts named as MFC-X-Cu. The gas adsorption experiments demonstrated that the MFC-X-Cu catalysts had equivalent CO_2 capture capacity compared to similar composites, and the contribution analysis of adsorption capacity revealed the interaction between the catalysts and CO_2 molecules. Furthermore, the structures and active sites of the catalysts were analyzed by various characterizations, and the possible mechanism of the MFC-X-Cu catalyzed cycloaddition reaction was proposed. In addition, the efficiency of the catalysts in catalyzing the cycloaddition of CO_2 with epoxides was investigated. The applicability and reusability of catalysts were also evaluated. This strategy will offer a green and sustainable pathway for CO_2 utilization.

2. Experimental section

2.1. Materials

The source of MF was the flagship store of Ledian on the Alibaba E-commerce platform. Copper (II) chloride dehydrate (AR) was purchased from Tianjin Yongda Reagent Co., Ltd. Sodium borohydride (98 wt%), styrene oxide (SO, 98 wt%), phenylglycidyl ether (99 wt%) and tetrabutylammonium bromide (TBAB, 99 wt%) were purchased from Shanghai Titan Technology Co., Ltd. 1,2-Epepoxytetradecane (95 wt%) was purchased from Shanghai Macklin Biochemical Co., Ltd. Epichlorohydrin (99 wt%) was purchased from Tianjin Fuchen Chemical Reagent Co., Ltd. Allyl glycidyl ether (99 wt%) was purchased from Shanghai Aladdin Biochemical Technology Co., Ltd. Tert-butyl glycidyl ether (96 wt%) was purchased from Beijing J&K Technology Co., Ltd. 1,2-Epoxyhexane (97 wt%) was purchased from Shanghai Energy Chemical Co., Ltd. CO_2 (99.99%) and N_2 (99.99%) were purchased from Nanchang Huasheng Gas Co. Ltd. All reagents were used directly without any additional purification.

### 2.2. Preparation of MFC-X-Cu materials

Scheme 1 depicts the preparation of MFC-X-Cu materials. Firstly, fresh MF was alternately immersed in ethanol and deionized water, followed by ultrasonication in each solution for 30 min. This cleaning process was repeated three times to effectively remove grease and surface impurities. The treated MF samples were desiccated in a blast drying oven at 80 °C for 12 h, and then cut into small squares. Subsequently, the small squares were placed on a quartz boat and then inserted into a tubular furnace for calcination. The temperature was initially increased from room temperature at a rate of 8 °C/min to 900 °C and held for 1 h. After the device cooled to room temperature, some black sponge-like solids named as MFC-900 were obtained, where 900 represents calcination temperature. Similarly, MFC-700, MFC-800, and MFC-1000 were synthesized using the same procedure. Next, 50 mg of MFC-900 was added to 10 mL of 0.01 mol/L $CuCl_2 \cdot 2H_2O$ solution in a 50 mL beaker. Then, 20 mL of 0.05 mol/L $NaBH_4$ was slowly added dropwise into the beaker above and stirred for 1 h. The mixture was subjected to solid liquid separation and then dried at 80 °C for 24 h. Finally, the dried black sponge-like solids were crushed in a mortar and named as MFC-900-Cu. The synthesis procedures of MFC-700-Cu, MFC-800-Cu, and MFC-1000-Cu were as the same as the MFC-900-Cu. In addition, catalysts including Cu-MFC-900 and Cu_2O-MFC-900 were prepared for comparison in the study. For the preparation of the Cu-MFC-900 catalyst, 50 mg of MFC-900 was initially submerged in a suspension of Cu powder, and the additional amount of Cu was determined based on the ICP results of MFC-900-Cu. The mixture was then stirred for 12 h and subsequently dried under vacuum. A similar method was followed to obtain the Cu_2O-MFC-900 catalyst as well.

2.3. Characterizations of MFC-X-Cu materials

X-ray diffraction (XRD) analysis was performed on a Rigaku RINT-2200 X-ray diffractometer. The device was equipped with a Cu Kα radiation operating at 40 kV and 20 mA. The scanning parameters of this device included a rate of 10° per minute and a scanning angle that extended from 10° to 80°. The specific surface and pore size distribution of samples was obtained on a Micromeritics TriStar II 3020 device. Moreover, the CO_2 adsorption isotherms of MFC-X-Cu were also tested on the Micromeritics TriStar II 3020 device, and detailed information was supplied in the section of S1.1 in Supporting Information. The morphological information of samples was analyzed by scanning electron microscope (SEM, HITACHI S-3400N) and transmission electron microscopy (TEM, JEOL JEM-2100). The crystal structure of metals was analyzed by high-resolution transmission electron microscopy (HRTEM, JEOL JEM-2100). X-ray photoelectron spectroscopy (XPS) characterization was carried out on an AXIS Supra of Kratos Analytical instrument. Fourier-transformed infrared spectral (FT-IR) was conducted on a Nicolet6700 FTIR spectrometer. Raman spectra of samples were collected on a LabRAM HR spectrometer. Temperature-programmed desorption (TPD, Micromeritics Autochem II 2920) instrument was used to analyze the acidic and basic sites of the samples in both quantitative and qualitative terms, and detailed parameters were provided in Supporting Information S1.2. The Cu content of samples was obtained on an inductively coupled optical emission spectrometer (ICP-OES, Agilent 720 ES). The N content and C content of samples were analyzed on an organic element analyzer (EuroVector, EA3000).

2.4. Cycloaddition of CO_2 with styrene oxide

In a typical cycloaddition reaction, 2 mmol of SO, 30 mg of MFC-X-Cu catalyst, and 30 mg of TBAB were added sequentially in a
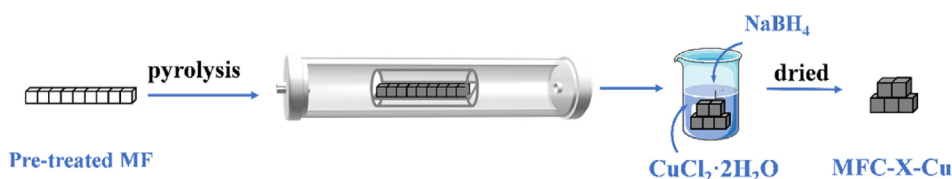
Scheme 1. The synthesis process of MFC-X-Cu catalysts.

25 mL PTFE-lined autoclave reactor. Pure CO_2 gas was purged into the reactor 5 times and then kept at initial pressure of 3 bar. Next, the reactor program was programmed to operate at a temperature of 110 °C for 3 h with a stirring speed of 600 rpm. The liquid products were analyzed by GC and GC-MS. The separated MFC-X-Cu catalyst was washed with ethanol three times and dried for the next run. Moreover, the yield and selectivity of the target product were calculated using the equations provided below:

$$Yield\ (\%) = \frac{n_2}{n_0}$$

$$Selectivity\ (\%) = \frac{n_2}{n_0 - n_1}$$

where n_0: molar amount of styrene oxide before the reaction; n_1: molar amount of SO after the reaction; and n_2: molar amount of styrene carbonate after the reaction.

3. Results and discussion

3.1. Structural characterizations

SEM and TEM characterizations were conducted to obtain detailed morphological and structural information of the catalysts. Fig. 1a and b and Fig. S1 show that the MFC-X and MFC-X-Cu catalysts are composed of intricately intertwined fibers forming three-dimensional structures, which contribute to frameworks with high porosity. The cross-sectional view of the branch break (encircled by the yellow dotted line in Fig. 1b) clearly shows that the branches have a hollow structure [29]. The enlarged section in the upper right corner provides a detailed view of the spherical connection points within the frameworks, which are crucial for structural stability. In terms of the overall morphology, the loading of copper component had no negative effect on the structure of the materials. The TEM images of the MFC-900 and MFC-900-Cu reveal the successful loading of Cu species in the material frameworks (Fig. 1c and d). Moreover, the HRTEM image of MFC-900-Cu shows discernible lattice fringes spaced approximately 0.24 nm apart, which corresponds to the (111) crystal plane of Cu_2O (shown in the inset of Fig. 1d) [30]. Furthermore, the EDS mapping images (Fig. 1e−i) of the MFC-900-Cu catalyst exhibited the uniform distribution of C, N, O, and Cu elements.

The N_2 adsorption and desorption analysis were employed to elucidate the porous structural properties of the MFC-X-Cu catalysts. Fig. 2a displays the N_2 adsorption-desorption isotherms of the catalysts, showing distinct hysteresis loops characteristic of type IV isotherms [31]. Notably, the MFC-800-Cu, MFC-900-Cu, and MFC-1000-Cu catalysts demonstrate significant adsorption at the low relative pressure P/P_0, primarily due to microporous filling. According to non-local density functional theory (NLDFT) curve analysis (Fig. 2b), these catalysts show a pore size distribution concentrated in the range of 1.5−2.5 nm, emphasizing their micro-mesoporous characteristics. The specific surface area, pore volume, and average pore size data for these catalysts are detailed in Table 1.

The specific surface areas of MFC-X-Cu catalysts increase with the calcination temperature, as evidenced by the values of 59 m²/g, 298 m²/g, 431 m²/g and 502 m²/g for MFC-700-Cu, MFC-800-Cu, MFC-900-Cu, and MFC-1000-Cu, respectively. This trend can be explained by the substantial gas generation from the MFC during the calcination process, leading to the development of additional pore structures in the material matrix. Notably, this phenomenon becomes more prominent at higher calcination temperature. Furthermore, the average pore sizes of the MFC-X-Cu catalysts, ranging from 2.27 to 6.48 nm, confirm the presence of mesoporous structures in the catalysts.

The structures of MFC-X-Cu catalysts were analyzed through XRD characterization, as shown in Fig. 3a. The XRD patterns of MFC-X-Cu catalysts reveal a broad peak at $2\theta = 25.6°$, indicating the presence of amorphous carbons and a degree of disorder within the carbon components of the catalysts [32]. Moreover, the sharp peaks centered at 36.5°, 42.2°, 61.5°, and 73.6° are assigned to the (111), (200), (311), (200) crystalline planes of Cu_2O (PDF#05-0667), respectively [33]. Furthermore, the peaks at $2\theta = 50.3°$ and 43.2° correspond to the Cu (111) and Cu (200) crystalline planes (PDF#04-0836), respectively [34]. The above results corroborate the successful integration of Cu and Cu_2O within the MFC materials, thereby confirming the adept synthesis of the MFC-X-Cu catalysts. Meanwhile, an increase in calcination temperature leads to a noticeable enhancement in the intensity of the crystalline peaks associated with both amorphous carbon and copper species.

Raman analysis was employed to obtain structural information of MFC-X-Cu catalysts by analyzing the scattered light resulting from molecular vibrations and rotations. Fig. 3b presents the Raman spectra of MFC-800-Cu, MFC-900-Cu, and MFC-1000-Cu. The prominent peaks at 1314 cm⁻¹, known as the D peaks, indicate the presence and intensity of disordered or amorphous carbon structures, such as defects, edges, and grain boundaries in the materials. In contrast, the G peaks are another characteristic feature of carbon materials in the Raman spectrum, which means the abundance of ideally ordered graphite or graphene structures within the material. The ratios of these peaks are referred to as I_D/I_G and provide important insight into the defect density and degree of graphitization in carbon materials [35]. According to Fig. 3b, the ID/IG ratios for the three catalysts were found to be 1.17, 1.15, and 1.14, indicating reduced defect sites and increased graphitization at higher catalyst calcination temperatures. It's interesting to note that the research has already focused on the critical role of defect sites in metal-carbon materials and the degree of graphitization in the capture and transformation of CO_2 [36,37].

XPS analysis was utilized to determine the surface chemistry of MFC-800-Cu, MFC-900-Cu, and MFC-1000-Cu catalysts. As shown in Fig. S2, the survey spectrum identifies the presence of C, N, O, and Cu in all catalysts. Detailed relative surface elemental contents can be found in Table S1. Among the catalysts, MFC-1000-Cu exhibits the lowest surface contents of Cu and N elements, with values of 1.31 at.% and 0.75 at.%, respectively. In contrast, MFC-900-Cu shows the highest surface Cu content at 3.73 at.%, while its surface N content is comparable to MFC-800-Cu, with values of 9.41 at.% and 9.95 at.%, respectively. It is noted
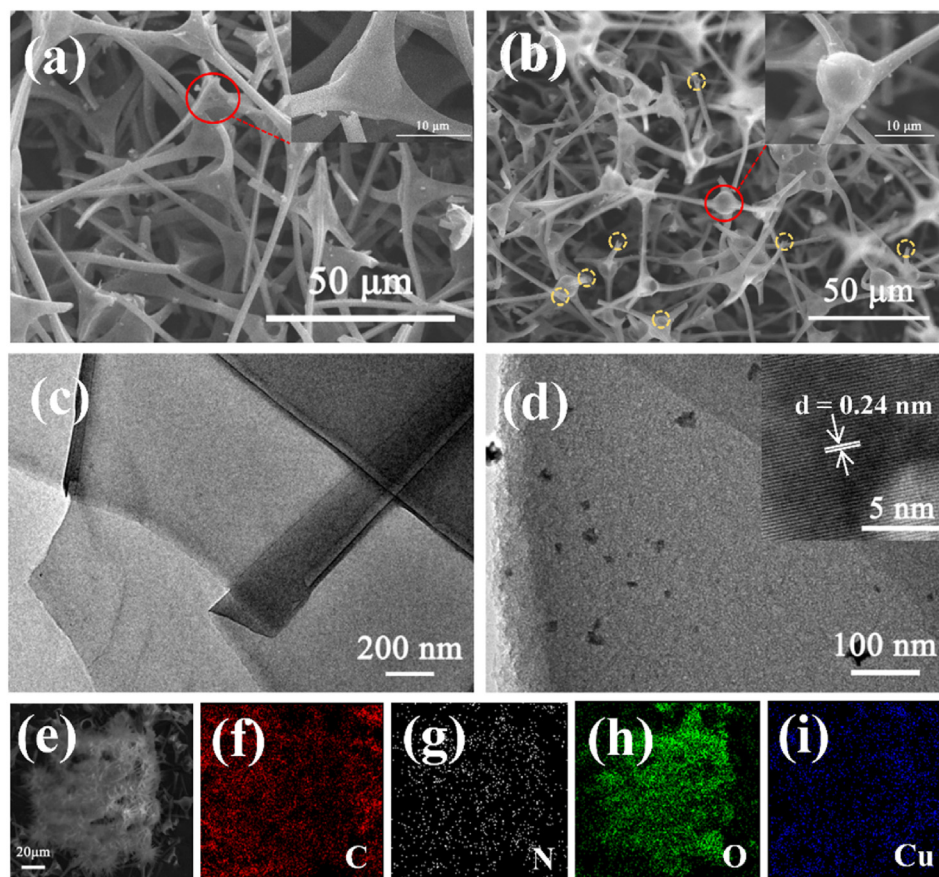
Fig. 1. SEM images of (a) MFC-900, (b) MFC-900-Cu, (c) TEM image of MFC-900, (d) TEM and HRTEM (inset) images of MFC-900-Cu, (e−i) EDS mapping images of MFC-900-Cu.
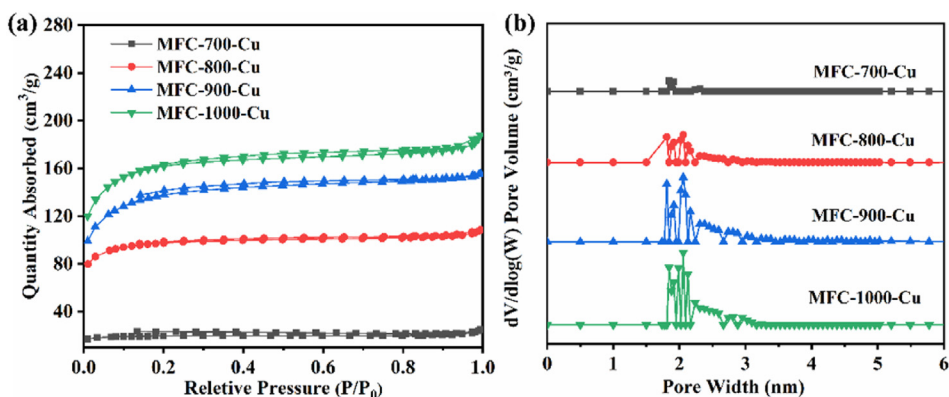

Fig. 2. (a) N_2 adsorption-desorption isotherms, (b) pore width curves of MFC-700-Cu, MFC-800-Cu, MFC-900-Cu, and MFC-1000-Cu catalysts.

Table 1
The structural features, elemental content, and CO_2 capture capacities of MFC-X-Cu samples.

Sample	S_{BET} (m²/g)	V_p (cm³/g)	D_{ave} (nm)	Elemental content (wt %)			CO_2 uptake (mmol/g)	
				C[a]	N[a]	Cu[b]	0 °C	25 °C
MFC-700-Cu	59	0.03	6.48	45.75	17.45	8.47	2.19	1.47
MFC-800-Cu	298	0.12	3.09	46.05	13.81	8.73	2.21	1.79
MFC-900-Cu	431	0.13	2.45	54.65	7.59	9.56	2.69	1.95
MFC-1000-Cu	502	0.16	2.27	50.23	4.75	10.26	2.44	1.71

[a] The content of C and N was obtained by elemental analysis.
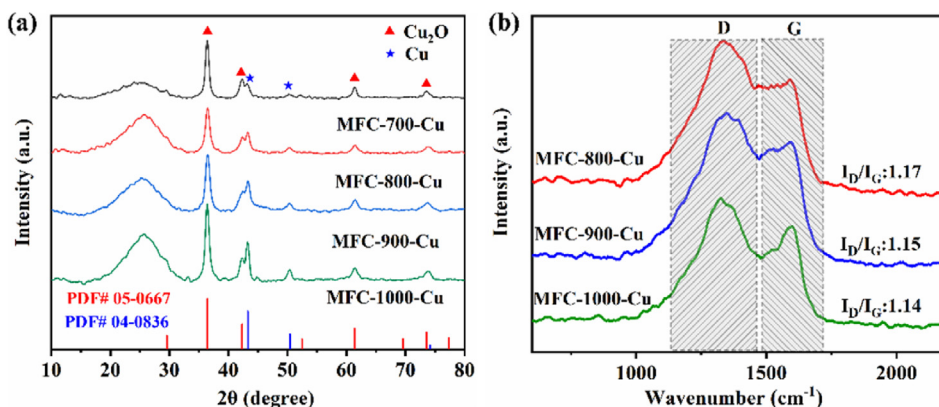[b] The content of Cu was measured by ICP-OES.

Fig. 3. (a) XRD patterns of MFC-X-Cu catalysts, (b) Raman spectra of MFC-800-Cu, MFC-900-Cu and MFC-1000-Cu catalysts.

that the apparent elemental content differs from the actual elemental mass fraction (Table 1), which is related to the structural properties of the material as well as the range of the characterization methods used. Moreover, Fig. 4a and b present the XPS spectrum for Cu 2p and N 1s, respectively. In Fig. 4a, the peaks near 932 eV and 952 eV are attributed to Cu $2p_{3/2}$ and Cu $2p_{1/2}$, respectively, and were deconvoluted for a more detailed analysis of the results [38]. The deconvoluted peaks at 932.48 eV and 952.29 eV are associated with Cu(0)/Cu(I) species [39]. However, the binding energies of Cu(0) and Cu(I) species overlap, which makes it impossible to clearly identify their species via XPS analysis alone [40]. In fact, the previous XRD patterns of MFC-X-Cu catalysts (Fig. 3a) have confirmed the presence of Cu and Cu_2O species. Furthermore, the peaks at 934.48 eV and 954.68 eV indicate the presence of Cu(II) species [41]. It is noteworthy that the absence of peaks of Cu(II) species in the XRD patterns could be due to the low crystallinity of these species. The N1s spectra (Fig. 4b) were deconvoluted into four N species: pyridinic N (398.23 eV), pyrrolic N (398.96 eV), graphitic N (400.87 eV), and oxidized N (403.8 eV) [42]. The relative contents of these four N species are listed in Table S3. The significant contribution of basic species (pyridinic and pyrrolic N) to CO_2 adsorption is well established. The results indicate that the relative contents of pyridinic and pyrrolic N in MFC-900-Cu and MFC-800-Cu catalysts are comparably high at 59.6% and 55.5%, respectively. In contrast, MFC-1000-Cu exhibited the lowest relative contents of these N species, with a value of only 45.8%. The elemental content and valence species on the surface are believed to alter the ability of the catalysts to capture and activate CO_2.

3.2. Interaction between CO_2 and MFC-X-Cu catalysts

The CO_2 adsorption capacities of the MFC-X-Cu catalysts at 0 °C and 25 °C under 1 bar are shown in Fig. 5a and b. Table 1 gives the maximum CO_2 adsorption capacities of these catalysts under the specified conditions. Among the tested catalysts, MFC-900-Cu exhibited the highest CO_2 adsorption capacity at 0 °C and 25 °C, with capacities of 2.69 and 1.95 mmol/g, respectively. To further confirm the effect of the MFC-900-Cu catalyst on CO_2 molecules, fresh and CO_2-adsorbed MFC-900-Cu catalysts were analyzed by FT-IR (Fig. S3). In the FT-IR spectra of CO_2-adsorbed MFC-900-Cu, two distinct peaks were observed at 2337 cm^{-1} and 2362 cm^{-1}. The peak at 2362 cm^{-1} is attributed to the asymmetric stretching vibration of CO_2 molecules weakly adsorbed on the catalyst surface. Conversely, the peak at 2337 cm^{-1} represents a stronger interaction between CO_2 molecules and the catalyst surface [43]. In addition, it is noteworthy that all MFC-X-Cu catalysts displayed non-linear isothermal curves with clear inflection points at lower pressures, which suggests that their interaction with CO_2 goes beyond mere physical adsorption [25]. To further explore this interaction, empirical equations were used to fit the CO_2 absorption isotherms of the MFC-X-Cu materials as described in section S1.3 of the Supporting Information. The fitted curves for MFC-900-Cu at 0 °C and 25 °C are shown in Fig. 5c and d, respectively, with the corresponding curves for MFC-700-Cu, MFC-800-Cu, and MFC-1000-Cu presented in Fig. S4. The high goodness of fit ($R^2 > 0.99$) of all fitted curves to the experimental data indicates a strong correlation, and the detailed parameters are provided in Table S2. Based on the fitting results, it can be inferred that chemical adsorption is
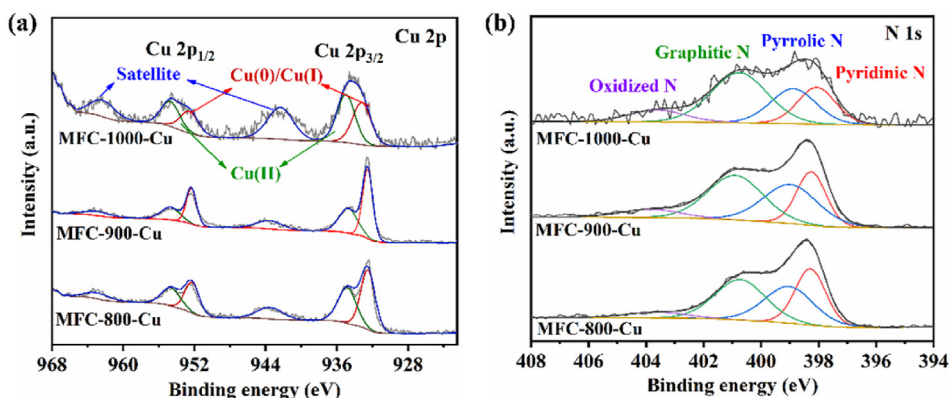

Fig. 4. XPS spectra of (a) Cu 2p and (b) N1s for MFC-800-Cu, MFC-900-Cu and MFC-1000-Cu catalysts.
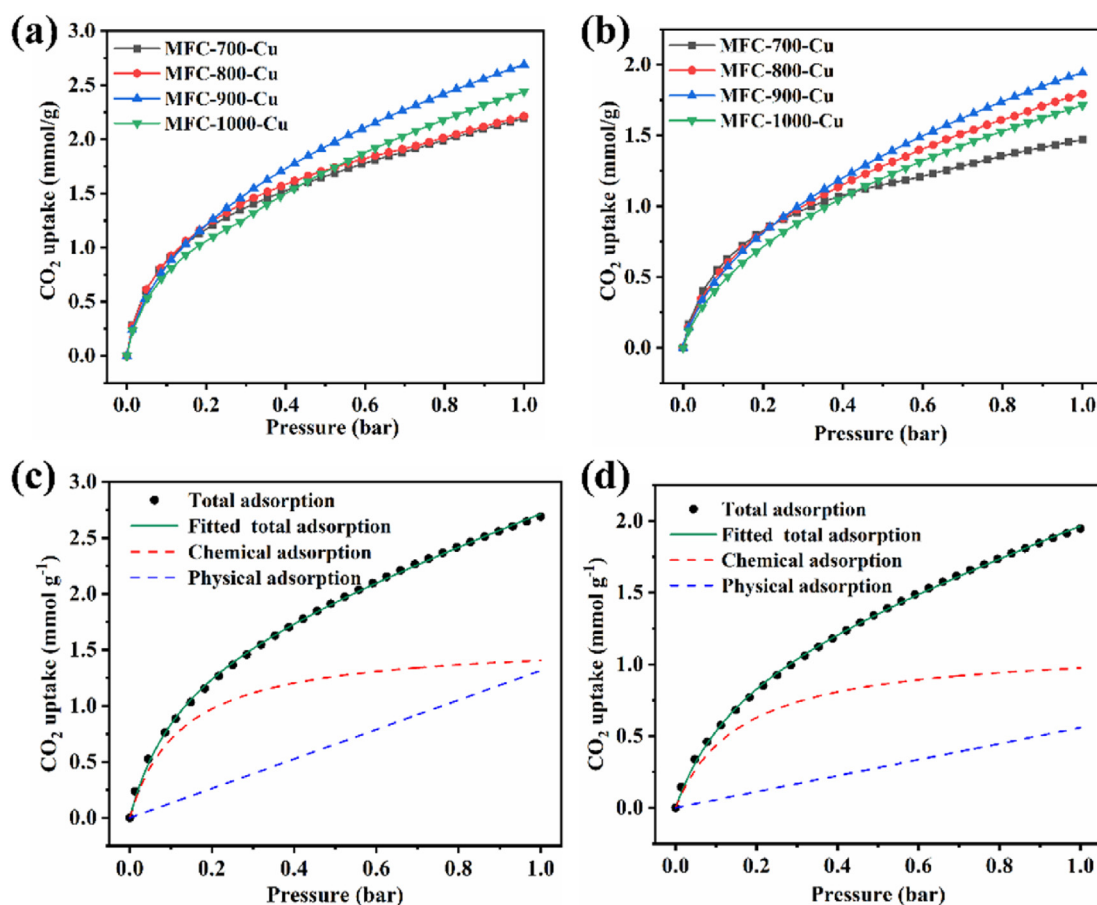
Fig. 5. CO_2 capture isotherms of MFC-X-Cu catalysts at 1 bar and (a) 0 °C (b) 25 °C. The fitted total, chemical, and physical adsorption curves of MFC-900-Cu (c) at 0 °C and (d) at 25 °C.

predominant at low pressures (0−0.2 bar), while physical adsorption prevails as the pressure increases. These findings were consistent with the conclusion of FTIR spectra (see Fig. S3). Notably, the MFC-1000-Cu displayed a lower slope in the chemisorption curves from 0 to 0.2 bar, suggesting weaker CO_2 chemisorption. This could be due to its lower contents of N and metal. In the low-pressure range (0−0.2 bar), the MFC-700-Cu and MFC-800-Cu catalysts adsorbed a similar capacity of CO_2 as MFC-900-Cu. However, within a pressure span of 0.2−1 bar, they exhibited lower CO_2 adsorption abilities compared to MFC-900-Cu. This disparity may be attributed to the higher specific surface area of MFC-900-Cu at 431 m^2/g, which exceeds that of MFC-700-Cu at 59 m^2/g and MFC-800-Cu at 298 m^2/g. The enhanced CO_2 adsorption capacity of MFC-900-Cu can be explained by its relatively larger specific surface area and higher N and Cu content, demonstrating a more favorable interaction with CO_2 molecules.

The acidity and basicity strength of the MFC-900-Cu catalyst were analyzed using CO_2-TPD and NH_3-TPD, as shown in Fig. 6a and b. It is widely recognized that the number of desorption peaks signifies the quantity of adsorbed species on a solid surface with different adsorption strengths, while the temperatures of desorption peaks represent the adsorption strengths of these species. Specifically, the desorption temperature intervals of chemisorbed CO_2 and NH_3 are used to deduce the surface base and acid strengths of the carriers, respectively. Fig. 6a shows that MFC-900-Cu has a narrow peak at 119 °C and a broad peak at 363 °C, indicating the presence of both weakly basic and moderately basic sites. This observation aligns with the prior findings from XPS analysis [44].

The abundance of basic sites enhances the CO_2 adsorption capacity of the MFC-900-Cu material. Moreover, the presence of weak and moderate-strong basic sites suggests that CO_2 can be easily desorbed at high temperatures, which is beneficial for subsequent recycling processes. Meanwhile, Fig. 6b reveals strong desorption peaks at 136 °C and 340 °C, signifying the existence of two types of acidic centers, which may be associated with the loaded Cu species. In conclusion, the hollow structure of the MFC-900-Cu catalyst, combined with its abundant basic and acidic sites enables highly efficient CO_2 capture and subsequent conversion.

3.3. Cycloaddition of CO_2

The cycloaddition of CO_2 represents a pivotal strategy for the valorization of CO_2 into value-added chemicals. In this work, the catalyst MFC-X-Cu was employed to catalyze the cycloaddition of CO_2 with epoxides, resulting in high value-added cyclic carbonates. The catalytic performance of various MFC-X-Cu catalysts is presented in Table 2. Owing to its exceptional CO_2 capture capacity, MFC-900-Cu was selected as a reference catalyst for the optimization of cycloaddition reaction parameters. The results indicated that elevating the CO_2 pressure from 1 bar to 3 bar led to a substantial increase in the production of cyclic carbonate, with the yield rising from 35% to 98% (Table 2, entries 1−3). The screening of reaction time and temperature revealed that a duration of 3 h at a temperature of 110 °C could achieve a yield of 98% and a selectivity of 99% for the cyclic carbonate product (Fig. S5). Furthermore, the reduction in both catalyst and TBAB dosages by half resulted in a
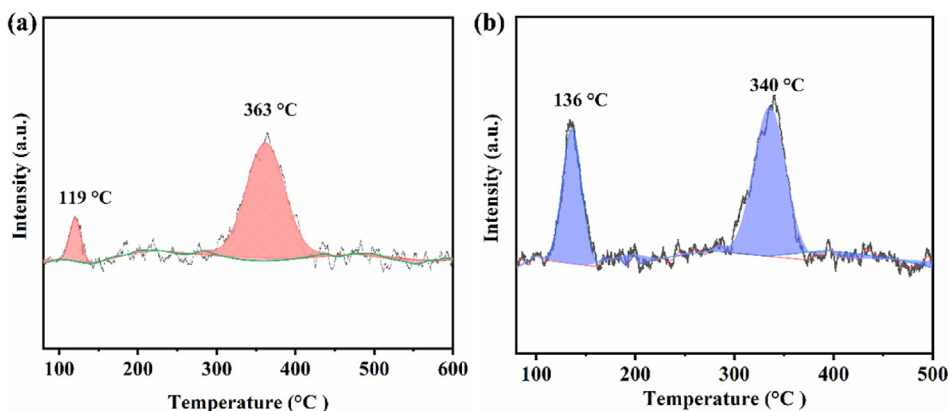
Fig. 6. (a) CO_2-TPD profiles and (b) NH_3-TPD profiles of MFC-900-Cu catalyst.

Table 2
Catalytic cycloaddition reaction of SO with CO_2 over MFC-X-Cu catalysts.[a]

Entry	Catalysts	CO_2/bar	Temp./°C	Yield/%	Selectivity/%
1	MFC-900-Cu	1	110	35 ± 1.65	98 ± 0.42
2	MFC-900-Cu	2	110	78 ± 2.05	99 ± 0.02
3	MFC-900-Cu	3	110	98 ± 0.59	99 ± 0.03
4[b]	MFC-900-Cu	3	110	60 ± 2.86	98 ± 0.64
5[c]	MFC-900-Cu	3	110	21 + 3.62	97 ± 0.92
6	MFC-900	3	110	52 ± 1.73	99 ± 0.06
7	TBAB	3	110	31 ± 4.75	98 ± 0.48
8	MFC-700-Cu	3	110	62 ± 2.95	98 ± 0.59
9	MFC-800-Cu	3	110	52 ± 1.63	99 ± 0.11
10	MFC-1000-Cu	3	110	66 ± 3.84	99 ± 0.38

[a] Reaction conditions: SO (2 mmol), MFC-X-Cu (30 mg), TBAB (30 mg), 3 h.
[b] MFC-900-Cu (15 mg), TBAB (15 mg).
[c] With the addition of 5 mg $CuCl_2 \cdot 2H_2O$ during the synthesis of MFC-900-Cu catalyst.

diminished yield of 38% from the original (Table 2, entries 3, 4). Therefore, the optimal reaction conditions for further evaluation involve a 3h duration at 110 °C, with 3 bar of CO_2, along with 30 mg of catalysts and TBAB. The study also examined the role of the Cu content in the catalyst. The catalytic performance was dropped to 21% when the quantity of $CuCl_2 \cdot 2H_2O$ in the catalyst was reduced to 5 mg, underscoring the pivotal role of Cu species in facilitating the CO_2 cycloaddition reaction (Table 2, entry 5). In comparison, the catalytic performance of the metal-free MFC-900 precursor was also tested with a yield of 52% (Table 2, entry 6). According to XRD patterns, it can be inferred that there were two kinds of Cu species including Cu^0 and Cu_2O in the MFC-900-Cu catalyst. To determine the active Cu species, Cu-MFC-900 and Cu_2O-MFC-900 catalysts were prepared with a post-impregnation method. The XRD patterns of Cu-MFC-900 and Cu_2O-MFC-900 indicated their successful synthesis (Fig. S6). Moreover, the corresponding catalytic performance of Cu-MFC-900 and Cu_2O-MFC-900 catalysts are listed in Table S4. The results showed that Cu-MFC-900, Cu_2O-MFC-900, and MFC-900-Cu catalysts displayed moderate catalytic activities at 90 °C, yielding cyclic carbonates at rates of 57%, 45%, and 53%, respectively. Notably, a significant improvement in the catalytic yields was observed at 110 °C, achieving 82%, 87%, and 98%, respectively. Therefore, these catalytic results support previous findings regarding the beneficial contribution of N and both Cu^0 and Cu_2O species within the catalyst framework to CO_2 cycloaddition. Additionally, the use of a single TBAB catalyst resulted in a meager yield of only 31% (Table 2, entry 7), highlighting the effectiveness of the MFC-X-Cu material in activating the reaction substrate. Subsequently, the catalytic performance of MFC-700-Cu,

MFC-800, and MFC-1000 was evaluated under the optimized conditions, with the yield of cyclic carbonates in 62%, 52%, and 66%, respectively (Table 2, entries 8–10). Characterization studies have implicated that the catalytic results are related to their structural properties and the distribution of accessible acidic and basic sites. It was concluded that the catalytic performance of the cycloaddition is not unilaterally determined by a single competitive advantage, such as high specific surface area, multiple metal loadings, and high N content. Overall, the MFC-900-Cu catalyst exhibited highly efficient synergistic effects for the activation of CO_2 and epoxides in cycloaddition reactions.

To gain a deeper understanding of the nature of the cycloaddition catalyzed by the MFC-X-Cu catalysts, it is crucial to explore the mechanism of this reaction. In conjunction with previous reports [45,46], we propose a possible mechanism for the CO_2 cycloaddition reaction as depicted in Scheme 2. Initially, CO_2 molecules are adsorbed and activated by an MFC-900-Cu catalyst. At the same time, the epoxides are activated through intermolecular forces between their oxygen atoms and the active metal centers on the surface of MFC-X-Cu catalysts [47,48]. Subsequently, the β-carbon of the epoxides is attacked by nucleophiles, forming an
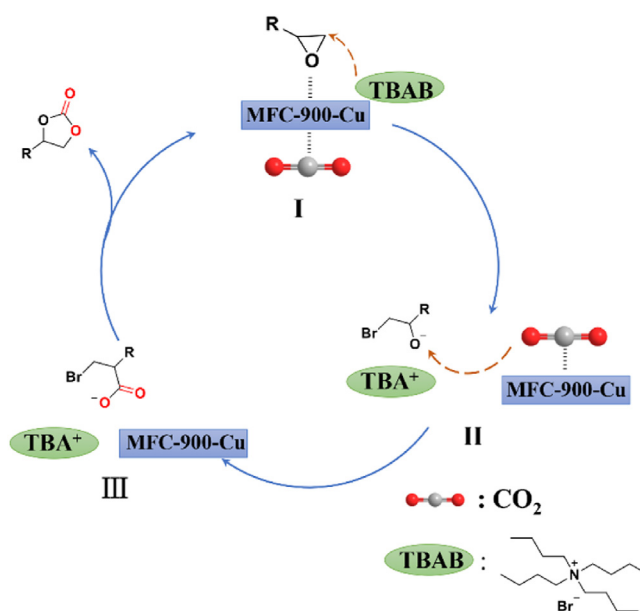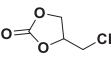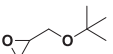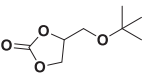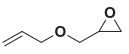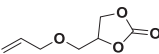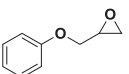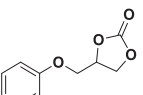

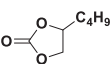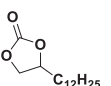**Scheme 2.** Proposed mechanism for the chemical fixation of CO_2 catalyzed by MFC-900-Cu.

intermediate bromoalkoxy compound in the presence of Br^- ions. Next, the CO_2 molecules are incorporated into the intermediate bromoalkoxy compounds, leading to the formation of alkyl carbonate anions, which are then converted into cyclic carbonate. Finally, MFC-900-Cu and TBAB are continuously involved in the catalytic cycle, ensuring that the reaction occurs efficiently and completely.

3.4. Applicability and reusability of MFC-900-Cu

The cycloaddition of CO_2 with various substrates was effectively catalyzed by MFC-900-Cu under optimized reaction conditions. Six epoxides with different functional groups were selected for the cycloaddition reactions and the results are summarized in Table 3. The results showed that substrates containing chlorine, ether, alkenyl, or phenyl groups gave yields over 98% (Table 3, entries 1–4). Furthermore, substrates with longer carbon chains also produced target cyclic carbonate with yields above 96% (Table 3, entries 5–6). These results demonstrate the significant applicability of MFC-900-Cu for cycloaddition reactions. In addition, the catalytic performance of MFC-900-Cu was further evaluated compared to other porous materials, as listed in Table S5. It is found that MFC-900-Cu not only has notable catalytic performance but also holds substantial potential for future applications.

In addition, the reusability of MFC-900-Cu was evaluated through the cycloaddition reaction of CO_2 and SO. As depicted in Fig. 7a, the catalytic efficiency of MFC-900-Cu remained largely consistent, even after five consecutive cycles. Various characterizations such as FT-IR, SEM, N_2 adsorption-desorption, ICP, and XRD were performed on the MFC-900-Cu samples before and after the cycling process to validate its stability (Fig. 7b and Fig. S7). The results indicated that the morphology and structural characteristics of MFC-900-Cu remained essentially unchanged. Although the specific surface area of the reused MFC-900-Cu catalyst decreased slightly from 431 m^2/g to 411 m^2/g, and the Cu content decreased from 9.56 wt% to 8.95 wt%, the catalyst exhibited good stability and reusability based on a comprehensive analysis of the experimental results and characterizations. These findings suggest the potential for industrial applications, which can promote the efficient conversion of CO_2 into commercially valuable compounds.

4. Conclusion

In summary, we have successfully synthesized a series of acid-base bifunctional catalysts (MFC-X-Cu) with hollow network structures and used them for the efficient capture and conversion of CO_2. The N species produced under high-temperature calcination of MF and the in-situ reduction-loaded Cu species provided both basic and acidic centers. Among the catalysts, MFC-900-Cu showed optimal performance in CO_2 capture and conversion. The superior catalytic activity of the MFC-900-Cu catalyst is attributed to its unique hollow porous structure and the synergistic effects of acid-base sites. This synergy improves the activation and subsequent conversion of CO_2 and epoxides. The FT-IR and CO_2/NH_3-TPD analysis further elucidated the interaction mechanisms between the catalysts and reaction substrate, highlighting the significant role of the basic N species and the acidic Cu species sites. Notably, MFC-900-Cu also exhibited good catalytic performance on the other epoxides substrates, achieving yields of 96%–99% for the target cyclic carbonates, indicating its good applicability. Furthermore, the MFC-900-Cu catalyst demonstrated great recyclability and maintained consistent catalytic efficiency over five cycles without significant loss of activity, demonstrating its potential for practical applications in CCU. Overall, the MFC-X-Cu catalysts offer a promising and sustainable solution for CO_2 capture and conversion.

Table 3
Catalytic activities of various epoxides over MFC-900-Cu catalyst.[a]

Entry	Substrate	Product	Yield/%	Selectivity/%
1			99	99
2			99	99
3			99	99
4			98	99
5			99	99
6			96	99

[a] Reaction conditions: Substrates (2 mmol), MFC-900-Cu (30 mg), TBAB (30 mg), CO_2 (3 bar), 110 °C, 3 h.
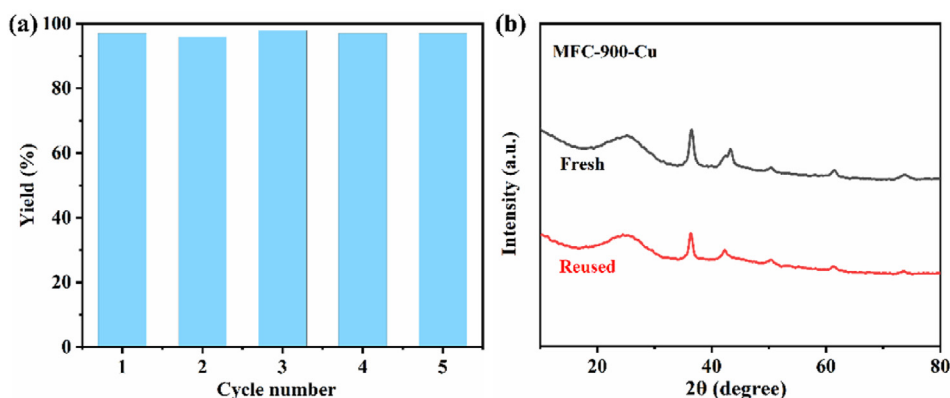

Fig. 7. (a) Reusability test of MFC-900-Cu, (b) XRD patterns of fresh and recycled MFC-900-Cu catalysts.

CRediT authorship contribution statement

Fei-Feng Mao: Writing − original draft, Investigation, Formal analysis. **Yu-Hua Dong:** Visualization. **Yan Zhou:** Resources, Methodology. **Ming-Shuai Sun:** Validation. **Wei Hui:** Writing − original draft, Supervision, Methodology, Writing − review & editing. **Duan-jian Tao:** Supervision, Project administration, Funding acquisition, Conceptualization, Writing − review & editing.

Declaration of competing interest

The authors declare that they have no known competing financial interests or personal relationships that could have appeared to influence the work reported in this paper.

Data availability

Data will be made available on request.

Acknowledgments

Appendix A. Supplementary data

Supplementary data to this article can be found online at https://doi.org/10.1016/j.mtener.2024.101677.

References

[1] F. Wang, J.D. Harindintwali, Z. Yuan, M. Wang, F. Wang, S. Li, Z. Yin, L. Huang, Y. Fu, L. Li, S.X. Chang, L. Zhang, J. Rinklebe, Z. Yuan, Q. Zhu, L. Xiang, D.C.W. Tsang, L. Xu, X. Jiang, J. Liu, N. Wei, M. Kästner, Y. Zou, Y.S. Ok, J. Shen, D. Peng, W. Zhang, D. Barceló, Y. Zhou, Z. Bai, B. Li, B. Zhang, K. Wei, H. Cao, Z. Tan, L.-b. Zhao, X. He, J. Zheng, N. Bolan, X. Liu, C. Huang, S. Dietmann, M. Luo, N. Sun, J. Gong, Y. Gong, F. Brahushi, T. Zhang, C. Xiao, X. Li, W. Chen, N. Jiao, J. Lehmann, Y.-G. Zhu, H. Jin, A. Schäffer, J.M. Tiedje, J.M. Chen, Technologies and perspectives for achieving carbon neutrality, Innovation 2 (2021) 100180. http://10.1016/j.xinn.2021.100180.
[2] S. Evro, B.A. Oni, O.S. Tomomewo, Global strategies for a low-carbon future: lessons from the US, China, and EU's pursuit of carbon neutrality, J. Clean. Prod. 461 (2024) 142635. http://10.1016/j.jclepro.2024.142635.
[3] C.H. Huang, C.S. Tan, A review: CO₂ utilization, Aerosol Air Qual. Res. 14 (2014) 480−499. http://10.4209/aaqr.2013.10.0326.
[4] J.M. Williams, D. Zhao, N. Zhang, S. Kawashima, A.J. Moment, Carboxylic ligands to enhance material recovery from construction waste to produce CaCO₃ for carbon utilization, Ind. Chem. Mater (2024). http://10.1039/d4im00025k.
[5] X. Hu, Y. Luo, X. Wu, J. Niu, M. Tan, Z. Sun, W. Liu, Heteroatom-doped microporous carbon nanosheets derived from pentaerythritol-melamine for supercapacitors and CO₂ capture, Mater. Today Energy 27 (2022) 101010. http://10.1016/j.mtener.2022.101010.
[6] Y. Sun, Y. Zhao, Y. Zhou, L. Wang, Z. Wang, J. Qi, D. Fu, P. Zhang, K. Zhao, Engineering the micro-structure for reducing energy consumption in CO₂ capture and catalytic conversion process, Mater. Today Energy 37 (2023) 101397. http://10.1016/j.mtener.2023.101397.
[7] Y. Gu, B.A. Anjali, S. Yoon, Y. Choe, Y.G. Chung, D.-W. Park, Defect-engineered MOF-801 for cycloaddition of CO2 with epoxides, J. Mater. Chem. A 10 (2022) 10051−10061. http://10.1039/d2ta00503d.
[8] C. Tangku, T. Saelee, M. Rittiruam, P. Khajondetchairit, S. Praserthdam, W. Anutrasakda, Y. Kuwahara, P. Praserthdam, Pd-loaded hierarchical titanosilicalite-1 catalysts on CO2 cycloaddition with epoxides: experimental and DFT investigations, Chemosphere 352 (2024) 141321. http://10.1016/j.chemosphere.2024.141321.
[9] C. Mosquera, A.L. Villa, Cycloaddition of limonene epoxide and CO₂ over Zn/SBA-15 catalysts for limonene carbonate synthesis, J. CO2 Util. 83 (2024) 102817. http://10.1016/j.jcou.2024.102817.
[10] B. Schäffner, F. Schäffner, S.P. Verevkin, A. Börner*, Organic carbonates as solvents in synthesis and catalysis, Chem. Rev. 110 (2010) 4554−4581. http://10.1021/cr900393d.

[11] T. Yan, H. Liu, Z.X. Zeng, W.G. Pan, Recent progress of catalysts for synthesis of cyclic carbonates from CO₂ and epoxides, J. CO2 Util. 68 (2023) 102355. http://10.1016/j.jcou.2022.102355.
[12] C. Guo, W. Liao, Z. Li, L. Sun, C. Chen, Easy conversion of protein-rich enoki mushroom biomass to a nitrogen-doped carbon nanomaterial as a promising metal-free catalyst for oxygen reduction reaction, Nanoscale 7 (2015) 15990−15998. http://10.1039/c5nr03828f.
[13] J. Cai, N. Lin, Y. Li, J. Xue, F. Li, L. Wei, M. Yu, X. Zha, W. Li, Research on the application of catalytic materials in biomass pyrolysis, J. Anal. Appl. Pyrolysis 177 (2024) 106321. http://10.1016/j.jaap.2023.106321.
[14] L. Leng, L. Yang, J. Chen, S. Leng, H. Li, H. Li, X. Yuan, W. Zhou, H. Huang, A review on pyrolysis of protein-rich biomass: nitrogen transformation, Bioresour. Technol. 315 (2020) 123801. http://10.1016/j.biortech.2020.123801.
[15] G. Nazir, A. Rehman, S. Hussain, Q. Mahmood, M. Fteiti, K. Heo, M. Ikram, M. Aizaz Ud Din, Towards a sustainable conversion of biomass/biowaste to porous carbons for CO2 adsorption: recent advances, current challenges, and future directions, Green Chem. 25 (2023) 4941−4980. http://10.1039/d3gc00636k.
[16] X. Wen, H. Liu, L. Zhang, J. Zhang, C. Fu, X. Shi, X. Chen, E. Mijowska, M.-J. Chen, D.-Y. Wang, Large-scale converting waste coffee grounds into functional carbon materials as high-efficient adsorbent for organic dyes, Bioresour. Technol. 272 (2019) 92−98. http://10.1016/j.biortech.2018.10.011.
[17] X. Wen, C. Li, H. Liu, G. Fan, Y. Tang, C. Hao, L. Ma, P. Song, Green carbonization of waste coffee grounds into porous C/Fe hybrids for broadband and high-efficiency microwave absorption, J. Mater. Sci. Technol. 170 (2024) 1−10. http://10.1016/j.jmst.2023.05.073.
[18] Y. Wang, Z. Chen, Y. Lu, L. Yang, T. Xu, H. Wu, J. Zhang, L. He, A review of application, modification, and prospect of melamine foam, Nanotechnol. Rev. 12 (2023) 20230137. http://10.1515/ntrev-2023-0137.
[19] X. Wu, Y. Qiu, W. Cai, J. Li, D. Wu, L. Xu, Y. Kong, Melamine foam supported NiCo2S4/Ag nanowires with charging/discharging induced activation effect for asymmetric supercapacitors, Chem. Eng. J. 484 (2024) 149667. http://10.1016/j.cej.2024.149667.
[20] M. Inagaki, M. Toyoda, Y. Soneda, T. Morishita, Nitrogen-doped carbon materials, Carbon 132 (2018) 104−140. http://10.1016/j.carbon.2018.02.024.
[21] Q. Lv, W. Si, J. He, L. Sun, C. Zhang, N. Wang, Z. Yang, X. Li, X. Wang, W. Deng, Y. Long, C. Huang, Y. Li, Selectively nitrogen-doped carbon materials as superior metal-free catalysts for oxygen reduction, Nat. Commun. 9 (2018) 1−11. http://10.1038/s41467-018-05878-y.
[22] Y. Xu, C. Wang, P. Niu, Z. Li, L. Wei, G. Yao, F. Zheng, Q. Chen, Tuning the nitrogen-doping configuration in carbon materialsviasulfur doping for ultra-stable potassium ion storage, J. Mater. Chem. A 9 (2021) 16150−16159. http://10.1039/d1ta03811g.
[23] J. Yu, X. Sun, Nitrogen-doped carbon dots as acid−base bifunctional and efficient catalysts for the cycloaddition of CO₂ with epoxides, New J. Chem. 48 (2024) 4245−4252. http://10.1039/d4nj00014e.
[24] Z. Zhang, L. Yu, Y. Tu, R. Chen, L. Wu, J. Zhu, D. Deng, Unveiling the active site of metal-free nitrogen-doped carbon for electrocatalytic carbon dioxide reduction, Cell Rep. Phys. Sci. 1 (2020) 100145. http://10.1016/j.xcrp.2020.100145.
[25] L. Shi, K.-Y. Liao, Y.-H. Dong, Y.-A. Wang, Y. Zhou, X.-G. Yi, M.-S. Sun, W. Hui, D.-J. Tao, Hollow branched fiber hierarchical porous carbon as recyclable adsorbents and catalysts for efficient CO₂ capture and conversion, Sustainable Mater.Technol. 40 (2024) e00880. http://10.1016/j.susmat.2024.e00880.
[26] W. Zhao, M. Shen, Y. Zhu, X. Ren, X. Li, Insights into Synergy of copper and acid sites for selective catalytic reduction of NO with ammonia over zeolite catalysts, Catalysts 13 (2023) 301. http://10.3390/catal13020301.
[27] J. Wu, D. Jin, X. Ren, D. Cao, K. Wu, H. Xu, D. Cheng, Copper-induced formation of Lewis acid sites enhancing sulfated zirconia catalyzed i-butane normalization, J. Catal. 432 (2024) 115400. http://10.1016/j.jcat.2024.115400.
[28] Y. Shao, K. Sun, Q. Li, Q. Liu, S. Zhang, Q. Liu, G. Hu, X. Hu, Copper-based catalysts with tunable acidic and basic sites for the selective conversion of levulinic acid/ester to γ-valerolactone or 1,4-pentanediol, Green Chem. 21 (2019) 4499−4511. http://10.1039/c9gc01706b.
[29] Y. Li, X. Zhao, Y. Lin, P. Li, Y. Tao, Z. Wang, J. Ma, H. Xu, Y. Liu, Lightweight MXene/carbon composite foam with hollow skeleton for air-stable, high-temperature-resistant and compressible electromagnetic interference shielding, Carbon 206 (2023) 375−382. http://10.1016/j.carbon.2023.02.061.
[30] Z. Dong, L. Zhang, S. Wang, L. Luo, Direct visualization of dynamic atomistic processes of Cu₂O crystal growth through gas-solid reaction, Nano, Energy 70 (2020) 104527. http://10.1016/j.nanoen.2020.104527.
[31] E. Allahkarami, E. Allahkarami, M. Heydari, A. Azadmehr, A. Maghsoudi, Assessment of chromite ore wastes for methylene blue adsorption: isotherm, kinetic, thermodynamic studies, ANN, and statistical physics modeling, Chemosphere 358 (2024) 142098. http://10.1016/j.chemosphere.2024.142098.
[32] Y. Shang, Z. Liu, J. Dong, M. Yao, Z. Yang, Q. Li, C. Zhai, F. Shen, X. Hou, L. Wang, N. Zhang, W. Zhang, R. Fu, J. Ji, X. Zhang, H. Lin, Y. Fei, B. Sundqvist, W. Wang, B. Liu, Ultrahard bulk amorphous carbon from collapsed fullerene, Nature 599 (2021) 599−604. http://10.1038/s41586-021-03882-9.
[33] L. Pan, L. Dai, O.J. Burton, L. Chen, V. Andrei, Y. Zhang, D. Ren, J. Cheng, L. Wu, K. Frohna, A. Abfalterer, T.C.-J. Yang, W. Niu, M. Xia, S. Hofmann, P.J. Dyson, E. Reisner, H. Sirringhaus, J. Luo, A. Hagfeldt, M. Grätzel, S.D. Stranks, High carrier mobility along the [111] orientation in Cu₂O photoelectrodes, Nature 628 (2024) 765−770. http://10.1038/s41586-024-07273-8.

[34] Y. Dong, K. Wang, Y. Tan, Q. Wang, J. Li, H. Mark, S. Zhang, Synthesis and characterization of pure copper nanostructures using wood inherent architecture as a natural template, Nanoscale Res. Lett. 13 (2018) 1−8. http://10.1186/s11671-018-2543-0.

[35] L.M. Malard, M.A. Pimenta, G. Dresselhaus, M.S. Dresselhaus, Raman spectroscopy in graphene, Phys. Rep. 473 (2009) 51−87. http://10.1016/j.physrep.2009.02.003.

[36] Y. Li, L. Liu, H. Yu, Y. Zhao, J. Dai, Y. Zhong, Z. Pan, H. Yu, Synergy of developed micropores and electronic structure defects in carbon-doped boron nitride for CO_2 capture, Sci. Total Environ. 811 (2022) 151384. http://10.1016/j.scitotenv.2021.151384.

[37] M. Balamurugan, H.Y. Jeong, V.S.K. Choutipalli, J.S. Hong, H. Seo, N. Saravanan, J.H. Jang, K.G. Lee, Y.H. Lee, S.W. Im, V. Subramanian, S.H. Kim, K.T. Nam, Electrocatalytic reduction of CO_2 to ethylene by molecular Cu-complex immobilized on graphitized mesoporous carbon, Small 16 (2020) 2000955. http://10.1002/smll.202000955.

[38] L. Ding, F. Yan, Y. Zhang, L. Liu, X. Yu, H. Liu, Microflowers comprised of Cu/CuxO/NC nanosheets as electrocatalysts and horseradish peroxidase mimics, ACS Appl. Nano Mater. 3 (2019) 617−623. http://10.1021/acsanm.9b02156.

[39] G. Sun, S. Jia, X. Zhang, Z. Kang, M. Cui, B. Wang, B. Wang, D.-P. Yang, Anchoring Core−Shell Cu@Cu2O Nanoparticles to two-dimensional carbon nanosheets for bacterial disinfection, ACS Appl. Nano Mater. 4 (2021) 9831−9841. http://10.1021/acsanm.1c02233.

[40] M. Ye, T. Shao, J. Liu, C. Li, B. Song, S. Liu, Phase engineering of Cu@Cu2O core-shell nanospheres for boosting tandem electrochemical CO_2 reduction to C2+ products, Appl. Surf. Sci. 622 (2023) 156981. http://10.1016/j.apsusc.2023.156981.

[41] W. Zhang, M. Chen, Y. Luo, Y. He, S. Liu, Y. Ye, M. Wang, Y. Chen, K. Zhu, H. Shu, M. Liu, J. Hou, T. Duan, X. Wang, Utilizing 2D layered structure Cu-g-C3N4 electrocatalyst for optimizing polysulfide conversion in wide-temperature Li-S batteries, Chem. Eng. J. 486 (2024) 150411. http://10.1016/j.cej.2024.150411.

[42] Q. Wei, L. Wu, M. Zhu, Z. Wang, Z.-H. Huang, M.-X. Wang, Porous nitrogen-doped reduced graphene oxide-supported CuO@Cu2O hybrid electrodes for highly sensitive enzyme-free glucose biosensor, iScience 26 (2023) 106155. http://10.1016/j.isci.2023.106155.

[43] M. Mihaylov, K. Chakarova, S. Andonova, N. Drenchev, E. Ivanova, E.A. Pidko, A. Sabetghadam, B. Seoane, J. Gascon, F. Kapteijn, K. Hadjiivanov, Adsorption of CO2 on MIL-53(Al): FTIR evidence of the formation of dimeric CO2 species, Chem. Commun. 52 (2016) 1494−1497. http://10.1039/c5cc08677a.

[44] B.-H. Cheng, L.-J. Deng, J. Jiang, H. Jiang, Catalytic cycloaddition of CO_2 to epoxides by the synergistic effect of acidity and alkalinity in a functionalized biochar, Chem. Eng. J. 442 (2022) 136265. http://10.1016/j.cej.2022.136265.

[45] A.K. Gupta, N. Guha, S. Krishnan, P. Mathur, D.K. Rai, A three-dimensional Cu(II)-MOF with Lewis acid−base dual functional sites for chemical fixation of CO_2 via cyclic carbonate synthesis, J. CO2 Util. 39 (2020) 101173. http://10.1016/j.jcou.2020.101173.

[46] Y. Liu, L. Shi, M. Pudukudy, S. Li, T. Ye, S. Shan, T. Hu, W. Tariq, Y. Zhi, PIL@NENPs composite as a synergetic heterogeneous catalyst to enhance the efficiency of CO_2 cycloaddition with epoxides, Mol. Catal. 554 (2024) 113821. http://10.1016/j.mcat.2024.113821.

[47] N. Gupta Sahil, Cyclic carbonates: treasure of fine chemicals obtained from waste stream CO2 over carbon-based heterogeneous catalysts, Renew. Sustain. Energy Rev. (2024) 114297. http://10.1016/j.rser.2024.114297.

[48] H. Liu, W. Liu, G. Xue, T. Tan, C. Yang, P. An, W. Chen, W. Zhao, T. Fan, C. Cui, Z. Tang, G. Li, Modulating charges of dual sites in multivariate metal−organic frameworks for boosting selective aerobic epoxidation of alkenes, J. Am. Chem. Soc. 145 (2023) 11085−11096. http://10.1021/jacs.3c00460.